

## Two-dimensional plasmon in a metallic monolayer on a semiconductor surface: Exchange-correlation effects

Takeshi Inaoka,<sup>1,\*</sup> Tadaaki Nagao,<sup>2</sup> Shuji Hasegawa,<sup>3</sup> Torsten Hildebrandt,<sup>4</sup> and Martin Henzler<sup>4</sup>

<sup>1</sup>*Department of Materials Science and Technology, Faculty of Engineering, Iwate University, 4-3-5 Ueda, Morioka, Iwate 020-8551, Japan*

<sup>2</sup>*Institute for Materials Research, Tohoku University, 2-1-1 Katahira, Aoba-ku, Sendai 980-8577, Japan*

<sup>3</sup>*Department of Physics, Graduate School of Science, University of Tokyo, 7-3-1 Hongo, Bunkyo-ku, Tokyo 113-0033, Japan*

<sup>4</sup>*Institut für Festkörperphysik der Universität Hannover, Appelstrasse 2, D-30167, Hannover, Germany*

(Received 9 July 2002; published 30 December 2002)

Taking account of exchange-correlation (XC) effects, we investigate two-dimensional (2D) plasmons (PL's) in a metallic monolayer on a semiconductor surface. The energy dispersion and the energy-loss intensity of the 2D PL are calculated in close relation to a recent experiment by high-resolution electron energy-loss spectroscopy. We evaluate the XC effects by using the local-field-correction theory and by comparing the calculated results among (i) the random-phase approximation, (ii) the Hartree-Fock approximation, and (iii) the approximation originally formulated by Singwi, Tosi, Land, and Sjölander. We determine the electron density  $n_0$  and the electron effective mass  $m^*$  so that the results in (iii) accord with the experimental ones. Our calculations give a good description of the energy dispersion and the energy-loss intensity of the 2D PL and the PL decay due to single-particle excitations in the experiment. With an increase in wave number  $q$ , the exchange and correlation begin to lower the dispersion curve and make the 2D PL decay at a smaller  $q$  value. Our electron system has a high effective density, because it lies on a semi-infinite dielectric medium. However, owing to low dimensionality, the XC effects start to appear remarkably in the 2D PL with an increase in  $q$ .

DOI: 10.1103/PhysRevB.66.245320

PACS number(s): 73.20.Mf, 71.45.Gm, 79.20.Uv

### I. INTRODUCTION

The Si(111)-( $\sqrt{3}\times\sqrt{3}$ )-Ag surface can be formed by depositing one monolayer (ML) of Ag atoms on a Si(111)-(7×7) surface at temperatures higher than 250 °C (for comprehensive reviews, see Refs. 1–3). Here, 1 ML denotes an atom density equal to that of the topmost layer of the Si(111) face, namely,  $7.83\times 10^{14}$  atoms/cm<sup>2</sup>. There are still some dangling-bond states on the clean Si(111)-(7×7) surface, though the reconstruction from an ideally truncated surface into a (7×7) surface decreases the number of dangling bonds remarkably. When Ag atoms are adsorbed to create the ( $\sqrt{3}\times\sqrt{3}$ )-Ag surface, the Ag atoms make covalent bonds with surface Si atoms, leaving no dangling bonds on the surface. The ( $\sqrt{3}\times\sqrt{3}$ )-Ag surface is known to have three surface states,  $S_1$ ,  $S_2$ , and  $S_3$ .<sup>4,5</sup> The  $S_1$  state with the highest energy arises mostly from Ag 5*p* orbitals oriented towards the surface-parallel direction.<sup>6</sup> The  $S_1$  state is localized virtually in the topmost layer of Ag and Si atoms, and its band possesses a parabolic energy dispersion crossing the Fermi level  $E_F$ .<sup>4,5</sup> The  $S_1$ -state band provides an ideal two-dimensional (2D) system of conduction electrons. The conduction-electron character of the  $S_1$  states can be visualized in low-temperature scanning-tunneling-microscopy (STM) images from a ( $\sqrt{3}\times\sqrt{3}$ )-Ag domain surrounded by atomic steps or out-of-phase boundaries.<sup>7</sup> One can clearly observe the standing waves that result from interference of electronic waves impinging on and reflected from the steps or boundaries.

Here, we mention electron doping into the  $S_1$ -state band induced by additional Ag adsorption onto the ( $\sqrt{3}\times\sqrt{3}$ )-Ag surface. This suggests controllability of the electron density

by the extra Ag adsorption. The additional Ag atoms are adsorbed as monomers and constitute a so-called 2D adatom-gas phase, when additional Ag coverage is not high enough to start nucleating into three-dimensional (3D) islands.<sup>8,9</sup> The critical additional coverage for this nucleation is about 0.03 ML at room temperature. A tiny quantity of Ag adatoms of 0.01 ML or so causes a substantial downward shift of the  $S_1$ -state band relative to  $E_F$ , and consequently a significant increase in the electron density in this band.<sup>10</sup> As is observed by angle-resolved ultraviolet photoelectron spectroscopy (ARUPS), a minute amount of extra Ag atoms of 0.022 ML gives rise to a downward band shift of about 0.15 eV, which entails an electron-density increase from  $1.6\times 10^{13}$  to  $3.5\times 10^{13}$  cm<sup>-2</sup>.<sup>2,10</sup> This implies that the electron density is quite sensitive to a small quantity of extra Ag atoms and that the Ag deposition must be controlled very carefully to acquire an electron system inherent in the ( $\sqrt{3}\times\sqrt{3}$ )-Ag surface. The above increase in the electron density can be clearly observed as an enhancement of surface electron conductivity through the  $S_1$ -state band.<sup>8,10</sup>

Quite recently, we have clearly observed 2D plasmons (PL's) due to the  $S_1$ -state band by means of high-resolution electron energy-loss spectroscopy (HREELS).<sup>11,12</sup> The energy dispersion and the energy-loss intensity of the 2D PL have been obtained in a broad wave-number ( $q$ ) region, until the 2D PL enters a single-particle-excitation (SPE) continuum, namely, an electron-hole-pair excitation continuum, and decays immediately. The wavelength of each occupied conduction-electron state and that of each PL mode are both much longer than the lattice constants, because the Fermi wavelength of our electron system is several tens of ångströms long. Accordingly, the background lattice exerts no substantial influence on the 2D PL's. There is no essential difference in the  $q$  dependence of the PL energy and the PL

loss-peak intensity between the  $\overline{\Gamma K'}$  direction and the  $\overline{\Gamma M'}$  direction in the surface Brillouin zone. This implies an isotropic nature of the 2D PL. By a quick drop in the PL loss-peak intensity, we can definitely locate a  $q$  value where the above PL decay occurs.

Since the  $S_1$  state with a conduction-electron character is localized virtually in the topmost layer of Ag and Si atoms, the thickness of the 2D electron system of several ångströms is much smaller than the wavelength of each PL mode. Therefore, the finite thickness of the 2D electron system has no significant effect on the 2D PL. In addition, interband transitions make no substantial contribution to the 2D PL, because the small thickness of surface states involves a wide energy separation between the  $S_1$ -state band and another surface-state band. We have only to consider transitions in the  $S_1$ -state band. The plasmon composed of these transitions can be recognized to be an ideal 2D PL. As for doping of the Si substrate, it has negligible influence on the energy dispersion of the 2D PL whether the substrate is  $n$  type or  $p$  type.<sup>11,12</sup> This clarifies that the 2D PL observed originates not from a surface space-charge layer but the  $S_1$ -state band.

In light of the fact that our electron system is an ideal 2D one, it is a good approximation to assume that electrons are restricted to a uniform plane positively charged, namely, a jellium plane. As shown in Refs. 11 and 12, the random-phase approximation<sup>13</sup> (RPA) gives a reasonable explanation of the observed energy dispersion and decay of the 2D PL, because this approximation can represent both the 2D PL and the SPE continuum adequately. However, the RPA is equivalent to a dynamical Hartree approximation, and it takes no account of the exchange-correlation (XC) effects. Our electron system lies on a semi-infinite dielectric medium, which leads to a long effective Bohr radius and consequently a high effective density. It is well known that the exchange and correlation play no significant role in excitations in a 3D electron system with a high effective density. In 2D electronic excitations, however, the XC effects may continue to be important up to higher effective densities, because the electrons' freedom of movement is restricted to a plane. Because of the XC effects, the electrons steer clear of one another, and this behavior can be described by exchange and correlation holes. Using the local-field correction (LFC), we can incorporate these XC effects into the RPA scheme. As the wavelength of each PL mode becomes comparable to radii of the exchange and correlation holes, the presence of the exchange and correlation holes begin to operate to weaken the effective Coulomb potential. Singwi, Tosi, Land, and Sjölander (STLS) formulated a LFC theory for 3D electronic excitations where the LFC and the static structure factor are determined self-consistently.<sup>14,15</sup> Jonson reformulated this theory to examine 2D electronic excitations.<sup>16</sup> Gold proposed parameterized forms of the LFC for both unpolarized and polarized electron systems in two and three dimensions.<sup>17</sup> The LFC theory, often including a generalization to finite temperatures, has been widely employed to examine interacting electrons in an inversion layer,<sup>16</sup> a single quantum well,<sup>18</sup> and two neighboring quantum wells.<sup>19–24</sup>

In the present work, taking account of the XC effects, we investigate the 2D PL due to the  $S_1$ -state band, in close re-

lation to our recent experiment by HREELS in Refs. 11 and 12. By means of the LFC, we calculate the energy dispersion and the energy-loss intensity of the 2D PL, and compare the results among (i) the RPA, (ii) the Hartree-Fock (HF) approximation, and (iii) the self-consistent STLS approximation. In (ii), the LFC is calculated by integrating the static structure factor in the HF approximation with respect to the wave vector. We determine the electron density  $n_0$  and the electron effective mass  $m^*$  so that the calculated results in (iii) agree with the experimental results. The above comparative analysis elucidates the XC effects on the 2D PL. Furthermore, we examine the  $q$  dependence of the integrated intensity of the PL loss peak in the EEL spectrum that clearly shows the PL decay due to SPE's. Though our electron system has a high effective density, with an increase in  $q$ , the XC effects start to emerge conspicuously in the 2D PL owing to low dimensionality.

## II. THEORY

In this section, we describe a theoretical framework for our analysis. We examine excitations of a 2D conduction-electron system in the surface-state band. We assume that the conduction electrons are confined on a uniform plane that is positively charged due to additional Ag adatoms ionized or extra donor-type surface states and that lies on a semi-infinite dielectric medium described by a dielectric constant  $\epsilon_s$ . The positive charges due to ionized Ag adatoms or surface states could be spread out into a uniform distribution of positive charges, because our electron system has a high effective density. This is similar to a degenerate semiconductor where each carrier "sees" an ionized impurity screened well by other carriers. We employ the 2D version<sup>16</sup> of the STLS approximation<sup>14,15</sup> in order to take account of the XC effects in electronic excitations. Our calculations are concerned with such a low-temperature experiment<sup>11,12</sup> (temperature  $T = 90$  K) that we can neglect temperature effects involved in the Fermi-Dirac (FD) distribution function. Accordingly, we use a zero-temperature scheme where the FD distribution function becomes a step function.

We focus our attention on the dynamical response of our electron system to a periodic and oscillatory external potential with wave vector  $\mathbf{q}$  and angular frequency  $\omega$ . The induced electron density can be expressed as

$$\delta n(\mathbf{q}, \omega) = \chi_0(\mathbf{q}, \omega) V(\mathbf{q}, \omega), \quad (1)$$

in terms of a susceptibility  $\chi_0$  of a noninteracting electron system and an effective potential  $V$  due to the response. The susceptibility  $\chi_0$  is written in the form

$$\chi_0(\mathbf{q}, \omega) = 2 \int \frac{d^2 \mathbf{k}}{(2\pi)^2} \frac{f(\mathbf{k} + \mathbf{q}) - f(\mathbf{k})}{E(\mathbf{k} + \mathbf{q}) - E(\mathbf{k}) + \hbar \omega + i\eta}, \quad (2)$$

where  $E(\mathbf{k})$ ,  $f(\mathbf{k})$ , and  $\eta$  denote the energy dispersion of electrons given by  $E(\mathbf{k}) = \hbar^2 \mathbf{k}^2 / 2m^*$  with wave vector  $\mathbf{k}$ , the FD distribution function for electron state  $\mathbf{k}$ , and an infinitesimal positive constant, respectively. The  $\mathbf{k}$  integration in

Eq. (2) can be carried out analytically at  $T=0$ .<sup>13</sup> The effective potential  $V(\mathbf{q}, \omega)$  is given as a Fourier component of the following  $V(\mathbf{r}, \omega)$ :

$$\varepsilon_t V(\mathbf{r}, \omega) = U(\mathbf{r}, \omega) + \int d^2\mathbf{r}' K(\mathbf{r} - \mathbf{r}') \delta n(\mathbf{r}', \omega). \quad (3)$$

The dielectric constant  $\varepsilon_t$  defined by  $\varepsilon_t = (\varepsilon_s + 1)/2$  describes the polarization of the semi-infinite dielectric medium. The potential  $U(\mathbf{r}, \omega)$  signifies an oscillating external potential, and the second term on the right-hand side (r.h.s.) of Eq. (3) divided by  $\varepsilon_t$  indicates an induced potential. The gradient of the kernel  $K$  is expressed as

$$\nabla K(\mathbf{r}) = g(\mathbf{r}) \nabla(e^2/r). \quad (4)$$

The static pair-correlation function  $g(\mathbf{r})$  in equilibrium represents many-body effects, namely, the exchange and correlation holes that result from the fact that electrons try to stay away from a near neighborhood of one another within a radius  $\sim k_F^{-1}$ . Here, the symbol  $k_F$  designates the Fermi wave number. The function  $g(\mathbf{r})$  can be related to the static structure factor  $S(\mathbf{k})$  by

$$g(\mathbf{r}) = 1 + \frac{1}{n_0} \int \frac{d^2\mathbf{k}}{(2\pi)^2} \{S(\mathbf{k}) - 1\} \exp(i\mathbf{k} \cdot \mathbf{r}), \quad (5)$$

where  $n_0$  stands for the uniform electron density in the absence of the external potential. With the aid of Eqs. (4) and (5), we can obtain the following equation from Eq. (3):

$$\varepsilon_t V(\mathbf{q}, \omega) = U(\mathbf{q}, \omega) + v(\mathbf{q}) \{1 - G(\mathbf{q})\} \delta n(\mathbf{q}, \omega). \quad (6)$$

The potential  $v(\mathbf{q})$  is expressed as  $v(\mathbf{q}) = 2\pi e^2/q$ . This is a 2D Fourier transform of the Coulomb potential  $e^2/r$ . The LFC  $G(\mathbf{q})$  is written as

$$G(\mathbf{q}) = \frac{1}{n_0} \int \frac{d^2\mathbf{k}}{(2\pi)^2} \frac{\mathbf{q} \cdot \mathbf{k}}{qk} \{1 - S(\mathbf{q} - \mathbf{k})\}. \quad (7)$$

The effects of the exchange and correlation holes are incorporated in  $G(\mathbf{q})$  through  $S(\mathbf{k})$ . The susceptibility  $\chi(\mathbf{q}, \omega)$  of an interacting electron system is defined by

$$\delta n(\mathbf{q}, \omega) = \chi(\mathbf{q}, \omega) U(\mathbf{q}, \omega), \quad (8)$$

and it involves the XC effects. Combining Eqs. (1), (6), and (8) yields the relation between  $\chi_0(\mathbf{q}, \omega)$  and  $\chi(\mathbf{q}, \omega)$ :

$$\chi(\mathbf{q}, \omega) = \frac{\chi_0(\mathbf{q}, \omega)}{\varepsilon_t - v(\mathbf{q}) \{1 - G(\mathbf{q})\} \chi_0(\mathbf{q}, \omega)}. \quad (9)$$

At  $T=0$ , the static structure factor  $S(\mathbf{q})$  can be exactly expressed as the following integration of  $\chi(\mathbf{q}, \omega)$ :<sup>25</sup>

$$S(\mathbf{q}) = -\frac{\varepsilon_t \hbar}{\pi n_0} \text{Im} \left[ \int_0^\infty d\omega \chi(\mathbf{q}, \omega) \right], \quad (10)$$

where  $\text{Im}$  denotes the imaginary part. We can obtain the  $q$  dependence of  $G(\mathbf{q})$  and  $S(\mathbf{q})$  by solving Eqs. (7), (9), and (10) self-consistently. These equations constitute a framework of the STLS approximation.

We regain the RPA by setting  $G(\mathbf{q})$  to be identically zero in the above scheme. The RPA takes no account of the XC effects. There is also a LFC based on the HF approximation.<sup>16</sup> In this scheme, we calculate  $G(\mathbf{q})$  by substituting into Eq. (7) the static structure factor in the HF approximation given by Eq. (8) in Ref. 16. Once  $G(\mathbf{q})$  is known, we can obtain  $\chi(\mathbf{q}, \omega)$  by Eq. (9). This correction takes only account of the  $X$  effect.

For convenience of numerical integration in Eq. (10), we make analytical continuation of  $\chi(\mathbf{q}, \omega)$  to the complex  $\omega$  plane, and convert the integral in real  $\omega$  in Eq. (10) into that in imaginary  $\omega$ .<sup>21</sup> This so-called Wick rotation allows us to avoid calculational difficulties due to plasmon poles on the real  $\omega$  axis.

The dielectric function  $\varepsilon(\mathbf{q}, \omega)$  is defined by

$$V_H(\mathbf{q}, \omega) = U(\mathbf{q}, \omega) / \varepsilon(\mathbf{q}, \omega), \quad (11)$$

where the Hartree potential  $V_H(\mathbf{q}, \omega)$  is given by

$$\varepsilon_t V_H(\mathbf{q}, \omega) = U(\mathbf{q}, \omega) + v(\mathbf{q}) \delta n(\mathbf{q}, \omega). \quad (12)$$

In Eq. (11), we employ not  $V(\mathbf{q}, \omega)$  in Eq. (6) but  $V_H(\mathbf{q}, \omega)$  in Eq. (12), because we assume that external charges generating  $U$  do not have XC interactions with the electrons. From Eqs. (8), (11), and (12), we can express  $\varepsilon(\mathbf{q}, \omega)$  as

$$\varepsilon_t / \varepsilon(\mathbf{q}, \omega) = 1 + v(\mathbf{q}) \chi(\mathbf{q}, \omega). \quad (13)$$

Electronic excitations in our system involve the energy loss that is equivalent to the work performed by external charges against the induced Coulomb potential. The energy loss per unit time and per unit area is written as

$$W = \frac{\varepsilon_t}{\pi e^2} q \omega |U(\mathbf{q}, \omega)|^2 \text{Im} \left[ -\frac{1}{\varepsilon(\mathbf{q}, \omega)} \right]. \quad (14)$$

In view of this expression, we define the energy-loss function  $F_L(\mathbf{q}, \omega)$  by

$$F_L(\mathbf{q}, \omega) = \text{Im}[-1/\varepsilon(\mathbf{q}, \omega)]. \quad (15)$$

The function  $F_L$  plays a central role in calculating the loss intensity in the HREELS, as shown below.

Next, we turn our attention to the loss intensity in the HREELS (see Ref. 26 as a comprehensive reference). An incident electron produces an external Coulomb potential  $U$  at the surface, which gives rise to electronic excitations involving the energy loss. The probability of the probing electron undergoing an energy loss  $\hbar\omega$  (single loss) and entering an analyzer aperture can be written as

$$P(\omega) = \{1 + n_{PK}(\omega)\} \int_D d^2\mathbf{q} F_K(\mathbf{q}, \omega) F_L(\mathbf{q}, \omega), \quad (16)$$

where the kinematic factor  $F_K(\mathbf{q}, \omega)$  and the Planck distribution function  $n_{PK}(\omega)$  are expressed as

$$F_K(\mathbf{q}, \omega) = (q/8\pi^4 e^2 \hbar^2) |U(\mathbf{q}, \omega)|^2 \quad (17)$$

and

$$n_{PK}(\omega) = 1/\{\exp(\hbar\omega/k_B T) - 1\}, \quad (18)$$

respectively. The factor  $F_K$  depends upon the scattering process of the probing electron. The symbol  $k_B$  in Eq. (18) stands for the Boltzmann constant. The integrated region  $D$  on the  $\mathbf{q}$  plane in Eq. (16) is the one that corresponds to scattering into the analyzer aperture. We take a coordinate frame where the  $z$  axis is in the surface-normal direction with its origin at the surface plane, and the  $x$  axis is the intersection of the surface plane with the specular-scattering plane in the sense that  $O-x$  points toward the analyzer. We define angle  $\varphi$  by  $q_x = q \cos \varphi$  and  $q_y = q \sin \varphi$ . When the function  $F_L(\mathbf{q}, \omega)$  is isotropic with respect to  $\mathbf{q}$ , Eq. (16) can be converted into

$$P(\omega) = \{1 + n_{PK}(\omega)\} \int dq G_K(q, \omega) F_L(q, \omega), \quad (19)$$

where the function  $G_K(q, \omega)$  is defined by

$$G_K(q, \omega) = q \int_{R(q)} F_K(\mathbf{q}, \omega) d\varphi. \quad (20)$$

In Eq. (19), the function  $F_L(\mathbf{q}, \omega)$  is expressed merely as  $F_L(q, \omega)$ , to stress that it depends not on the direction of  $\mathbf{q}$  but only on the magnitude of  $\mathbf{q}$ . The integration in Eq. (19) is performed in a  $q$  range when  $\mathbf{q}$  moves in the above region  $D$ . The integrated range  $R(q)$  in Eq. (20) designates a  $\varphi$  range that corresponds to the intersection of a circle of radius  $q$  with the region  $D$  on the  $\mathbf{q}$  plane.

In the so-called dipole scattering mentioned above, it is a good approximation to assume that the incident electron follows a classical trajectory.<sup>27</sup> The scattered direction is sharply concentrated about the specular-reflection direction, and usually the energy loss  $\hbar\omega$  in the scattering is much smaller than the incident energy  $E_0$ . Accordingly, we employ a specular-reflection trajectory where the position of the probing electron at time  $t$  has its surface-parallel component  $\mathbf{V}t$  and its surface-normal one  $v_z|t|$ . Here, the symbols  $\mathbf{V}$  and  $v_z$  are a constant velocity vector and a positive constant velocity, respectively. In this treatment, the external potential is written as

$$U(\mathbf{q}, \omega) = \frac{4\pi e^2 v_z}{(\omega - \mathbf{q} \cdot \mathbf{V})^2 + (qv_z)^2}. \quad (21)$$

The probability  $P(\omega)$  in Eq. (19) obtained from Eq. (21) indicates the energy-loss probability when a probing electron travels along the (00) beam.

The analyzer aperture is located right at the center of the so-called dipole lobe, when it is adjusted to the specular-reflection direction. As the position of the aperture deviates from the specular-reflection direction, the aperture begins to collect intensity halfway down the dipole lobe, and the probed dispersion region shifts, as exhibited below. We treat this off-specular, namely, angle-resolved geometry.

### III. RESULTS AND DISCUSSION

By means of the theoretical framework in Sec. II, we investigate 2D PL's at the Si(111)-( $\sqrt{3} \times \sqrt{3}$ )-Ag surface in close relation to our recent HREELS experiment in Ref. 11. We compare our calculated results in three cases, namely, (i)

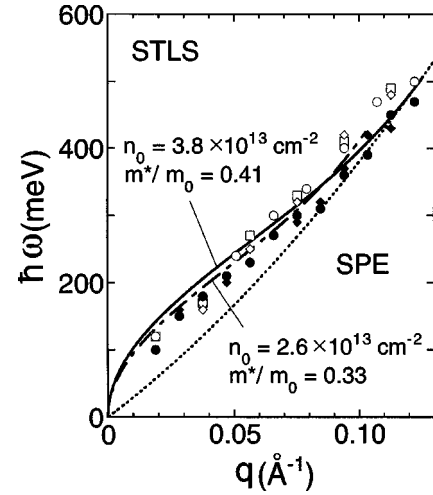


FIG. 1. Energy dispersion of the two-dimensional plasmon at the Si(111)-( $\sqrt{3} \times \sqrt{3}$ )-Ag surface. The solid curve and the dash-dotted one show the calculated results in the STLS approximation for the electron density  $n_0 = 3.8 \times 10^{13} \text{ cm}^{-2}$  and the electron effective-mass ratio  $m^*/m_0 = 0.41$  and for  $n_0 = 2.6 \times 10^{13} \text{ cm}^{-2}$  and  $m^*/m_0 = 0.33$ , respectively. The SPE continuum for the former set of  $n_0$  and  $m^*/m_0$  extends on the right side of the dotted curve. Several series of points of various shapes exhibit the experimental results obtained by the HREELS with different incident energies  $E_0$  along the  $\overline{\Gamma K'}$  and  $\overline{\Gamma M'}$  lines in the surface Brillouin zone (Ref. 11).

the RPA that takes no account of the XC effects,<sup>13</sup> (ii) the HF approximation that considers only the exchange effect,<sup>16</sup> and (iii) the STLS approximation that takes both the exchange and correlation effects into consideration.<sup>16</sup> We determine the electron density  $n_0$  and the effective electron mass  $m^*$  by fitting our calculated results in (iii) with the experimental results. With these parameter values determined, we calculate the other two cases (i) and (ii) as well for comparison.

Figure 1 shows the energy dispersion of the 2D PL calculated by the STLS approximation in comparison with that obtained by HREELS. The dispersion is given by zeros of the denominator in Eq. (9). A solid curve and a dash-dotted curve are the dispersion calculated for  $n_0 = 3.8 \times 10^{13} \text{ cm}^{-2}$  and  $m^*/m_0 = 0.41$  and that for  $n_0 = 2.6 \times 10^{13} \text{ cm}^{-2}$  and  $m^*/m_0 = 0.33$ , respectively. A dotted curve marks a boundary of the SPE continuum for  $n_0 = 3.8 \times 10^{13} \text{ cm}^{-2}$  and  $m^*/m_0 = 0.41$ , and the continuum extends on the right side of the dotted curve. At  $n_0 = 2.6 \times 10^{13} \text{ cm}^{-2}$ , the 2D PL reaches the SPE continuum at  $q \approx 0.10 \text{ \AA}^{-1}$  where the dash-dotted curve terminates, though the boundary of the continuum is not displayed in this figure. The 2D PL decays immediately, when it enters the SPE continuum. Several series of dots of various shapes exhibit the experimental results at a low temperature  $T = 90 \text{ K}$  for some different incident-energy values  $E_0$  and for two  $\mathbf{q}$  directions along the  $\overline{\Gamma K'}$  and  $\overline{\Gamma M'}$  lines. As mentioned in Ref. 11, there is no substantial difference in energy dispersion among these  $E_0$  values and between the two  $\mathbf{q}$  directions. The effective mass  $m^*$  has been adjusted by the method of least squares for each of the two  $n_0$  values. The energy of the 2D PL is not so sensitive to

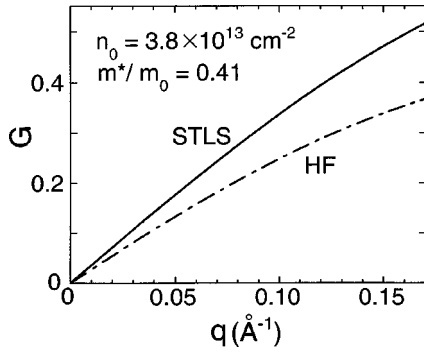


FIG. 2.  $q$  dependence of the local-field correction  $G$  in the STLS approximation (solid curve) and the Hartree-Fock approximation (dash-dotted curve) for  $n_0 = 3.8 \times 10^{13} \text{ cm}^{-2}$  and  $m^*/m_0 = 0.41$ .

the choice of  $n_0$ . However, it is evident that, at a larger  $n_0$  value,  $n_0 = 3.8 \times 10^{13} \text{ cm}^{-2}$ , the 2D PL decays away at a higher  $q$  value around  $0.125 \text{ \AA}^{-1}$ . As shown below, the loss-peak intensity due to the 2D PL in the EEL spectrum for  $n_0 = 3.8 \times 10^{13} \text{ cm}^{-2}$  declines quickly around the same  $q$  value, in good agreement with the experiment.

Here, we mention the effective density parameter  $r_s^*$  defined by  $\pi(r_s^* a_B^*)^2 n_0 = 1$  with the effective Bohr radius  $a_B^* = \epsilon_r \hbar^2 / m^* e^2$ . The radius  $a_B^*$  and the parameter  $r_s^*$  take values of  $a_B^* = 10.0 \text{ \AA}$  and  $r_s^* = 1.10$ , when  $n_0 = 2.6 \times 10^{13} \text{ cm}^{-2}$  and  $m^*/m_0 = 0.33$ , and those of  $a_B^* = 8.07 \text{ \AA}$  and  $r_s^* = 1.13$ , when  $n_0 = 3.8 \times 10^{13} \text{ cm}^{-2}$  and  $m^*/m_0 = 0.41$ . The presence of the semi-infinite dielectric medium with  $\epsilon_s = 11.5$  (Ref. 28) is responsible for a large  $a_B^*$  value, and consequently a small  $r_s^*$  value. The above  $r_s^*$  values close to unity indicate that our electron system has a high effective density.

From now on, we employ the values of  $n_0 = 3.8 \times 10^{13} \text{ cm}^{-2}$  and  $m^*/m_0 = 0.41$ , which leads to the Fermi wave number  $k_F = 0.155 \text{ \AA}^{-1}$  and the Fermi energy  $E_F = 222 \text{ meV}$  measured from the band bottom. Figure 2 exhibits the  $q$  dependence of  $G(\mathbf{q})$  in the STLS approximation (solid curve) and in the HF approximation (dash-dotted curve). With an increase in  $q$ , the  $G$  value rises from zero and increases monotonically. Owing to the XC effects, the electrons move clear of the close vicinity of one another within a radius  $\sim k_F^{-1}$ . The XC effects make no substantial contribution to  $V(\mathbf{q}, \omega)$  at  $q \approx 0$  where the wavelength is much longer than radii of the exchange and correlation holes. However, as the wavelength begins to become comparable to the hole radii with an increase in  $q$ , the XC effects start to operate to weaken the effective Coulomb interaction represented by the second term on the r.h.s. of Eq. (6). The  $G$  value in the STLS approximation is larger than that in the HF approximation, because the HF approximation includes only the exchange effect.

Figure 3 displays the energy dispersion of the 2D PL in the STLS approximation (solid curve), the HF approximation (dash-dotted curve), and the RPA (broken curve) for  $n_0 = 3.8 \times 10^{13} \text{ cm}^{-2}$  and  $m^*/m_0 = 0.41$ . The SPE continuum extends on the right side of the dotted curve. The PL decays quickly when it goes into the SPE continuum. This PL decay

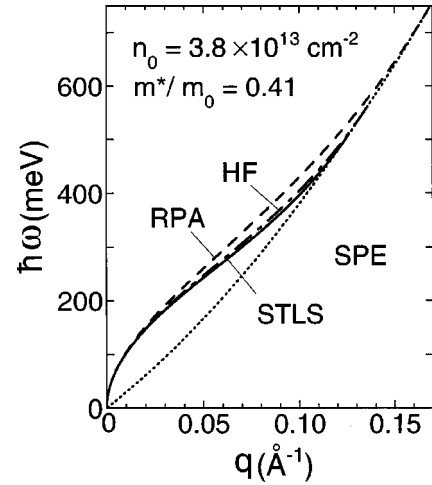


FIG. 3. Energy dispersion of the two-dimensional plasmon in the STLS approximation (solid curve), the Hartree-Fock approximation (dash-dotted curve), and the random-phase approximation (broken curve) for  $n_0 = 3.8 \times 10^{13} \text{ cm}^{-2}$  and  $m^*/m_0 = 0.41$ . The SPE continuum extends on the right side of the dotted curve.

occurs at a smaller  $q$  value in the STLS approximation than in the HF approximation, though it is not so obvious in this figure. This difference becomes quite evident in Fig. 4, as shown below.

The PL energy rises from zero as  $\sqrt{q}$  near  $q = 0$ , and there is no difference among the three approximations in this small  $q$  range. With an increase in  $q$ , however, the XC effects begin to operate to lower the PL energy and make the PL decay at a smaller  $q$  value, because the XC effects start to weaken the effective Coulomb interaction [see Eq. (6)]. We find a greater difference between the HF approximation and the RPA than between the STLS and HF approximations. This indicates that the exchange effect is more significant than the correlation effect.

Here, we focus our attention on the integrated energy-loss intensity  $I_{\text{PL}}$  of the 2D PL, namely, the resonance-peak area of the 2D PL in the  $\omega$  dependence of  $F_L$  at each  $q$  value. This quantity is related to the loss-peak intensity in the HREELS. The above resonance peak is represented by the Dirac  $\delta$  function in our calculational scheme. Figure 4 shows the  $q$  dependence of the integrated energy-loss intensity  $I_{\text{PL}}$  in the STLS approximation (solid curve), the HF approximation (dash-dotted curve), and the RPA (broken curve). Each of the three curves corresponds to one of the three curves in Fig. 3 according to the specification of its approximation name. With an increase in  $q$ , the intensity  $I_{\text{PL}}$  rises from zero, passes its maximum, and decreases to zero. There is no difference among the three approximations at the initial intensity rise where the PL energy exhibits the  $\sqrt{q}$  dispersion. The  $q$  value where the intensity drops to zero corresponds to the one where the energy-dispersion curve reaches the boundary of the SPE continuum. The XC effects make the intensity decline more rapidly and fall to zero at a conspicuously smaller  $q$  value. Figures 3 and 4 imply that the XC effects play a significant role in the 2D PL, though our electron system possesses a high effective density of  $r_s^* \approx 1$ . This is in clear contrast to the fact that the XC effects have no signifi-

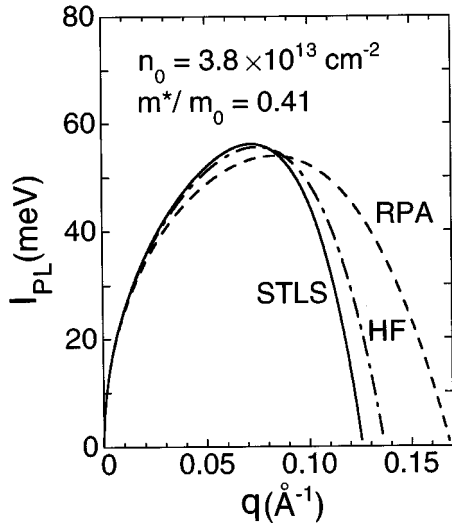


FIG. 4.  $q$  dependence of the integrated energy-loss intensity  $I_{\text{PL}}$  of the two-dimensional plasmon in the STLS approximation (solid curve), the Hartree-Fock approximation (dash-dotted curve), and the random-phase approximation (broken curve) for  $n_0 = 3.8 \times 10^{13} \text{ cm}^{-2}$  and  $m^*/m_0 = 0.41$ . The integrated intensity  $I_{\text{PL}}$  is defined by the resonance-peak area of the plasmon in  $\omega$  dependence of the energy-loss function at each  $q$  value.

cant influence on excitations in a 3D electron system with a high effective density. The XC effects originate from the fact that the electrons steer clear of the immediate proximity of each other. These effects are considered to appear more remarkably in a 2D system where electrons are constrained to a plane than in a 3D system.

Here, we turn our attention to the loss-peak intensity of the 2D PL in the EEL spectrum. In the experiment, initially we adjust the analyzer aperture to the specular-reflection direction, namely, to the center of the so-called dipole lobe. As we rotate the surface plane gradually, the center of the dipole lobe deviates from the analyzer aperture increasingly, or equivalently the aperture shifts down the tail of the dipole lobe. This shift of the aperture position entails that of the probed dispersion region.

The kinematic factor  $G_K$  in Eq. (19) involves the scattering process of the probing electron and depends upon the incident angle  $\alpha_0$ , the incident energy  $E_0$ , and the analyzer position. The angle  $\alpha_0$  is measured from the surface normal of the initial surface plane before rotation. The probed dispersion region is defined by a region on the  $q$ - $\omega$  plane where  $G_K$  takes substantial values. At each  $\omega$  value, the  $q$  dependence of  $G_K$  displays a one-peak structure, and we evaluate the probed  $q$  range by the full width at half maximum of the peak. By repeating this evaluation with change in  $\omega$ , we can obtain the probed dispersion region on the  $(q, \omega)$  plane. As a typical case, we rotate the surface plane by angle  $\beta$  by tilting the surface normal to a direction perpendicular to the scattering plane in the initial specular-reflection geometry. We assume a circular analyzer aperture with half angle  $\theta_a$ , and treat this angle as an adjustable parameter in the analysis below of the loss-peak intensity. Figure 5 shows the  $\beta$  dependence of the probed dispersion region for  $\alpha_0 = 6^\circ$  and

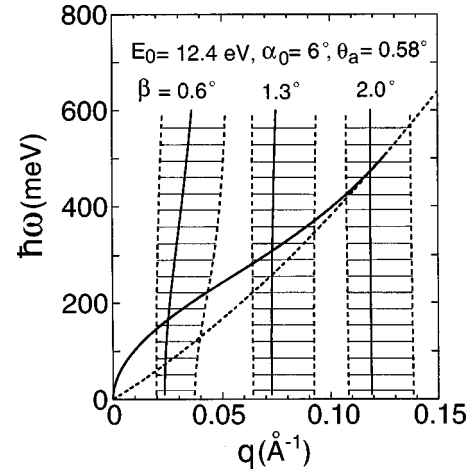


FIG. 5. Rotated-angle ( $\beta$ ) dependence of the probed dispersion region for the incident angle  $\alpha_0 = 6^\circ$ , the incident energy  $E_0 = 12.4 \text{ eV}$ , and the half-angle of the circular analyzer aperture  $\theta_a = 0.58^\circ$ . Each probed dispersion region is defined as a region on the  $(q, \omega)$  plane where the kinematic factor  $G_K$  in Eq. (19) takes substantial values. The surface plane of the material is rotated by the angle  $\beta$  by tilting the surface normal to a direction perpendicular to the scattering plane in the initial specular-reflection geometry. The solid curve and the dotted curve running from the origin are the same as those in Fig. 3.

$E_0 = 12.4 \text{ eV}$  corresponding to the experiment. As for  $\theta_a$ , we have used the value of  $\theta_a = 0.58^\circ$  adjusted below. Each hatched region with  $\beta$  specified indicates a probed dispersion region for this  $\beta$  value. There is a solid line passing inside each region. At each  $\omega$  value, the factor  $G_K$  reaches its maximum at a point where the horizontal line for this  $\omega$  value intersects with the above-noted passing line. The solid curve and the dotted curve, both starting from the origin, exhibit the energy dispersion of the 2D PL in the STLS approximation and the boundary of the SPE continuum, respectively. These two curves are the same as those in Fig. 3. With an increase in angle  $\beta$ , the probed dispersion region shifts to the higher  $q$  side. Each probed region extends in a direction nearly parallel to the  $\omega$  axis, when  $\alpha_0 (= 6^\circ)$  is small. At each  $\beta$  value, we can substantially observe a specific part of the dispersion curve that crosses the probed region. In the EEL spectrum, the loss peak emerges around an  $\omega$  value where the dispersion curve intersects with the above-stated passing line. With an increase in  $\beta$ , we can scan the energy dispersion, till the 2D PL decays away owing to SPE's.

The  $q$  dependence of  $F_L$  is constituted of a PL resonance peak in the  $\delta$ -function form, if present, and a weak and extending intensity distribution due to SPE's. We can derive the PL component in  $P(\omega)$  by making the  $q$  integration for the PL resonance peak in Eq. (19). By integrating the PL component in  $P(\omega)$  with respect to  $\omega$ , we can obtain the probability  $P_{\text{PL}}$  that a probing electron traveling along the (00) beam creates 2D PL's and becomes scattered into the analyzer aperture. When the incident direction is nearly normal ( $\alpha_0 = 6^\circ$ ), the probing electron interacts with the polarized surface in a short time, which leads to a small  $P_{\text{PL}}$  value much lower than unity. In view of this, in Fig. 6, we compare

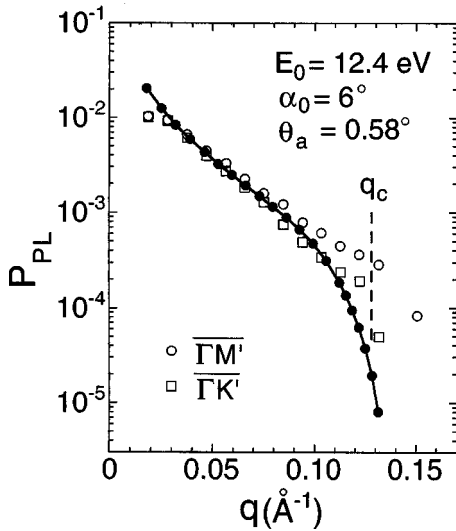


FIG. 6.  $q$  dependence of the calculated probability  $P_{\text{PL}}$  that an incident electron with  $\alpha_0=6^\circ$ ,  $E_0=12.4$  eV produces two-dimensional plasmons and enters a circular analyzer aperture with half-angle  $\theta_a=0.58^\circ$  (solid circles connected by lines), in comparison with the  $q$  dependence of the integrated intensity of the plasmon loss peak in the HREELS normalized by the integrated elastic-peak intensity along the  $\overline{\Gamma K'}$  line (open squares) and the  $\overline{\Gamma M'}$  line (open circles). The two-dimensional plasmon decays around  $q_c \approx 0.13 \text{ \AA}^{-1}$  due to single-particle excitations.

the calculated probability  $P_{\text{PL}}$  with the integrated loss-peak intensity of the 2D PL normalized by the integrated elastic-peak intensity in the HREELS. The aperture angle  $\theta_a$  has been determined by fitting the calculated result to the experimental one. A series of solid circles connected by lines exhibits the  $q$  dependence of the calculated probability  $P_{\text{PL}}$  with  $\theta_a=0.58^\circ$ . The ordinate is indicated in a logarithmic scale. The  $q$  value for each solid circle has been obtained from the intersection of the dispersion curve and the line passing inside the probed dispersion region, as displayed in Fig. 5. The open squares and the open circles represent the observed  $q$  dependence of the integrated PL-loss intensity normalized by the integrated elastic-peak intensity along the  $\overline{\Gamma K'}$  line and the  $\overline{\Gamma M'}$  line, respectively. As mentioned in Ref. 11, the experimental results imply that the 2D PL decays away around  $q_c \approx 0.13 \text{ \AA}^{-1}$ . Our calculation can reproduce quite well the experimental result, namely, the monotonic intensity decline with an increase in  $q$  and the rapid intensity drop around  $q_c$  due to the PL decay.

A decrease in  $\theta_a$  narrows the width of each probed dispersion region in Fig. 5, and brings about a nearly parallel downward shift and a sharper intensity drop around  $q_c$  in the  $P_{\text{PL}}$  curve in Fig. 6. However, the change in  $\theta_a$  has no substantial influence on the  $q_c$  value. The shape of the analyzer aperture in the experiment is not a circle but a rectangle, and the above value of  $\theta_a=0.58^\circ$  is close to a value of  $0.48^\circ$  estimated by the longer side of the rectangle.

The  $P_{\text{PL}}$  value declines with an increase in  $q$  even in a smaller  $q$  range of  $0.02 \text{ \AA}^{-1} \leq q \leq 0.07 \text{ \AA}^{-1}$  where the integrated PL intensity  $I_{\text{PL}}$  increases with  $q$  (see Fig. 4). To understand this decline, we recall that the probability  $P(\omega)$  can

be obtained by integrating the product of  $G_K$  and  $F_L$  with respect to  $q$ , as seen from Eq. (19). As the analyzer aperture shifts down the tail of the dipole lobe with an increase in  $\beta$ , the probed dispersion region transfers to the larger  $q$  side, and simultaneously the peak intensity in the  $q$  dependence of  $G_K$  in the probed region drops quite quickly. This quick drop in  $G_K$  is responsible for the above decline in  $P_{\text{PL}}$ , because it is more influential than the enhancement of  $I_{\text{PL}}$  obtained from  $F_L$ .

We have determined the values of  $n_0$  and  $m^*$  by fitting the calculated results in the STLS approximation with the experimental results of the HREELS. On the other hand, ARUPS measurements of the  $(\sqrt{3} \times \sqrt{3})$ -Ag surface are providing various values, namely,  $n_0 = (1.6 \pm 0.3) \times 10^{13} \text{ cm}^{-2}$  and  $m^*/m_0 = 0.29 \pm 0.05$  in Ref. 10, and  $n_0 = 0.9 \times 10^{13} \text{ cm}^{-2}$  and  $m^*/m_0 = 0.07$  in Ref. 29. These values are smaller than ours. There are even ARUPS data that imply that the bottom of the  $S_1$ -state band lies above  $E_F$  at the complete  $(\sqrt{3} \times \sqrt{3})$ -Ag surface without any extra Ag adatoms.<sup>30</sup> As stated in Sec. I, a minute quantity of additional Ag adatoms leads to a great increase in  $n_0$ . In addition, the electron density  $n_0$  may be sensitive to other impurities or surface states. Further experimental studies will be required to identify the  $S_1$ -state band for the complete  $(\sqrt{3} \times \sqrt{3})$ -Ag surface. Discrepancies in  $n_0$  and  $m^*$  among different experiments could be ascribed to different levels of electron doping into the  $S_1$ -state band by extra Ag adatoms, dopant impurities or donor-type surface states. Varying an amount of additional Ag adatoms carefully makes a significant difference in  $n_0$ .<sup>30</sup> This suggests that we could control  $n_0$  by careful deposition and temperature treatment. Irrespective of variable electron doping, at least, we can assert that an ideal 2D conduction-electron system with a high effective density can be realized at the  $(\sqrt{3} \times \sqrt{3})$ -Ag surface, and that, with an increase in  $q$ , the XC effects begin to appear in the 2D PL remarkably due to low dimensionality, in spite of the high effective density.

#### IV. SUMMARY

The  $S_1$ -state band at the  $\text{Si}(111)$ - $(\sqrt{3} \times \sqrt{3})$ -Ag surface provides an ideal two-dimensional conduction-electron system. Taking XC effects into consideration, we have examined the energy dispersion and the energy-loss intensity of the 2D PL due to the  $S_1$ -state band, in connection with our recent experiment by HREELS. We have employed the local-field-correction theory, and have evaluated the XC effects on the 2D PL by comparing the calculated results among the random-phase approximation, the Hartree-Fock approximation, and the STLS approximation. Our results can be summarized as follows:

(1) By choosing adequate values of the electron density  $n_0$  and the electron effective mass  $m^*$ , our calculations in the STLS approximation can reproduce quite well the energy dispersion and the loss-peak intensity of the 2D PL, and the PL decay owing to SPEs in the HREELS.

(2) At each  $n_0$  value chosen, the calculated dispersion has been adjusted to the observed one by varying  $m^*$ . The critical wave number  $q_c$  where the PL decay occurs depends

upon  $n_0$  significantly, though the PL energy is not so sensitive to  $n_0$ . Accordingly, we can determine  $n_0$  definitely by fitting the calculated  $q_c$  value to the observed one.

(3) As the wavelength of the 2D PL begins to become comparable to radii of exchange and correlation holes with an increase in wave number  $q$ , the XC effects start to lower the dispersion curve, and make the 2D PL decay away due to SPE's at a smaller  $q$  value.

(4) Our electron system has a high effective density of the effective density parameter  $r_s^* \approx 1$ , because it lies on a semi-infinite dielectric medium. However, because of low dimensionality, the XC effects emerge in the 2D PL conspicuously with an increase in  $q$ .

A significant variation in  $n_0$  and  $m^*$  among different ex-

periments could be attributed to different levels of electron doping into the  $S_1$ -state band by extra Ag adatoms, dopant impurities or donor-type surface states. This doping level could be controlled by careful deposition and treatment.

#### ACKNOWLEDGMENTS

This work was supported by a Grant-in-Aid for Scientific Research from the Ministry of Education, Science, Sport, and Culture under Grant No. 13640315. Numerical calculations in the present work were performed at the Information Synergy Center of Tohoku University and the Iwate University Super Computing and Information Sciences Center.

\*Corresponding author.

- <sup>1</sup>S. Hasegawa, X. Tong, S. Takeda, N. Sato, and T. Nagao, *Prog. Surf. Sci.* **60**, 89 (1999).
- <sup>2</sup>S. Hasegawa, N. Sato, I. Shiraki, C. L. Petersen, P. Bøggild, T. M. Hansen, T. Nagao, and F. Grey, *Jpn. J. Appl. Phys., Part 1* **39**, 3815 (2000).
- <sup>3</sup>S. Hasegawa and F. Grey, *Surf. Sci.* **500**, 84 (2002).
- <sup>4</sup>S. Hasegawa, X. Tong, C.-S. Jiang, Y. Nakajima, and T. Nagao, *Surf. Sci.* **386**, 322 (1997).
- <sup>5</sup>X. Tong, C.-S. Jiang, and S. Hasegawa, *Phys. Rev. B* **57**, 9015 (1998).
- <sup>6</sup>H. Aizawa and M. Tsukada, *Phys. Rev. B* **59**, 10 923 (1999).
- <sup>7</sup>N. Sato, S. Takeda, T. Nagao, and S. Hasegawa, *Phys. Rev. B* **59**, 2035 (1999).
- <sup>8</sup>Y. Nakajima, G. Uchida, T. Nagao, and S. Hasegawa, *Phys. Rev. B* **54**, 14 134 (1996).
- <sup>9</sup>N. Sato, T. Nagao, and S. Hasegawa, *Phys. Rev. B* **60**, 16 083 (1999).
- <sup>10</sup>Y. Nakajima, S. Takeda, T. Nagao, S. Hasegawa, and X. Tong, *Phys. Rev. B* **56**, 6782 (1997).
- <sup>11</sup>T. Nagao, T. Hildebrandt, M. Henzler, and S. Hasegawa, *Phys. Rev. Lett.* **86**, 5747 (2001).
- <sup>12</sup>T. Nagao, T. Hildebrandt, M. Henzler, and S. Hasegawa, *Surf. Sci.* **493**, 680 (2001).
- <sup>13</sup>F. Stern, *Phys. Rev. Lett.* **18**, 546 (1967).
- <sup>14</sup>K. S. Singwi, M. P. Tosi, R. H. Land, and A. Sjölander, *Phys. Rev. Lett.* **176**, 589 (1968).
- <sup>15</sup>K. S. Singwi and M. P. Tosi, in *Solid State Physics*, edited by H. Ehrenreich, F. Seitz, and D. Turnbull (Academic, New York, 1981), Vol. 36, p. 177.
- <sup>16</sup>M. Jonson, *J. Phys. C* **9**, 3055 (1976).
- <sup>17</sup>A. Gold, *Z. Phys. B: Condens. Matter* **103**, 491 (1997).
- <sup>18</sup>E. H. Hwang and S. Das Sarma, *Phys. Rev. B* **64**, 165409 (2001).
- <sup>19</sup>A. Gold, *Z. Phys. B: Condens. Matter* **86**, 193 (1992).
- <sup>20</sup>Chao Zhang, *Phys. Rev. B* **49**, 2939 (1994).
- <sup>21</sup>L. Zheng and A. H. MacDonald, *Phys. Rev. B* **49**, 5522 (1994).
- <sup>22</sup>J. Szymański, L. Świerkowski, and D. Neilson, *Phys. Rev. B* **50**, 11 002 (1994).
- <sup>23</sup>L. Liu, L. Świerkowski, D. Neilson, and J. Szymański, *Phys. Rev. B* **53**, 7923 (1996).
- <sup>24</sup>D. S. Kainth, D. Richards, H. P. Hughes, M. Y. Simmons, and D. A. Ritchie, *J. Phys.: Condens. Matter* **12**, 439 (2000).
- <sup>25</sup>D. Pines and P. Nozières, *The Theory of Quantum Liquids* (Benjamin, New York, 1966), Vol. 1.
- <sup>26</sup>H. Ibach and D. L. Mills, *Electron Energy Loss Spectroscopy and Surface Vibrations* (Academic, New York, 1982).
- <sup>27</sup>W. L. Schaich, *Phys. Rev. B* **24**, 686 (1981).
- <sup>28</sup>H. R. Philipp and H. Ehrenreich, *Phys. Rev.* **129**, 1550 (1963).
- <sup>29</sup>J. N. Crain, K. N. Altmann, C. Bromberger, and F. J. Himpsel, *Phys. Rev. B* **66**, 205302 (2002).
- <sup>30</sup>R. I. G. Uhrberg, H. M. Zhang, T. Balasubramanian, E. Landemark, and H. W. Yeom, *Phys. Rev. B* **65**, 081305(R) (2002).